1024x1024 LWIR SLS FPAs – Status and Characterization

Mani Sundaram[†], Axel Reisinger, Richard Dennis, Kelly Patnaude, Douglas Burrows, Jason Bundas, Kim Beech, Ross Faska, and Dan Manitakos
QmagiQ, 22 Cotton Road, Suite 180, Nashua, NH, USA 03063-4219

ABSTRACT

An infrared sensor technology that has made quick progress in recent years is the photodiode based on Type-II InAs/(In)GaSb strained layer superlattices (SLS). We have developed Focal Plane Arrays (FPAs) with up to a million pixels, quantum efficiency exceeding 50%, and cutoff wavelength ~ 10 microns. SLS offers the promise of the high quantum efficiency and operating temperature of longwave infrared mercury cadmium telluride (MCT) at the price point of midwave infrared indium antimonide (InSb). That promise is rapidly being fulfilled. This paper presents the current state-of-the-art of this sensor technology at this critical stage of its evolution.

Keywords: SLS, T2SL, Superlattices, InAs/GaSb, Longwave infrared, LWIR, FPA

1. INTRODUCTION

Type-II InAs/InGaSb strained layer superlattice (SLS) is a novel infrared sensor technology[1,2] with the theoretical promise of better performance than MCT[3] and InSb combined with the manufacturing ease and low cost of InSb and QWIP.

Recent progress in longwave infrared SLS photodiodes has been rapid[4-9], but work remains to be done before SLS can achieve its potential in a high-performance focal plane array (FPA) – high quantum efficiency (QE), high pixel operability and uniformity, higher operating temperature (than MCT with the same cutoff wavelength), good image stability, reproducibility, etc. If successful, the payoff would be significant.

Two fundamental areas requiring improvement are material quality and surface passivation of small pixels in large-format detector arrays, particularly as the cutoff wavelength is extended beyond 10 μm. Our efforts are focused on these areas.

2. TYPE-II STRAINED LAYER SUPERLATTICE MATERIALS

Using the bandgaps and offsets for the InAs/InSb/GaSb/AlSb material system (Fig. 1), quantum mechanics is used to calculate the electron and hole bandstructures and the effective bandgap of a sample InAs/GaSb superlattice in Fig. 2.

The electron and heavy-hole ground state wavefunctions graphed on the right of Fig. 2 show them to be mostly confined to alternate layers, with the heavy holes well localized in the GaSb layers.

This localization prevails for higher energy heavy-hole states also (Fig. 3), a consequence of the large heavy-hole mass as reflected in its flat dispersion relationship schematically sketched at the bottom of Fig. 2.

Fortunately, the extended electrons provide adequate wavefunction overlap and therefore optical absorption.

[†] Correspondence: Email: msundaram@qmagiq.com; Telephone: 603 821 3092 x200; Fax: 603 821 3094

One lesson from this modeling is to have electrons be the minority carriers, rather than holes. The electrons, being less localized, will have higher minority carrier lifetime and longer diffusion length, resulting in higher quantum efficiency.

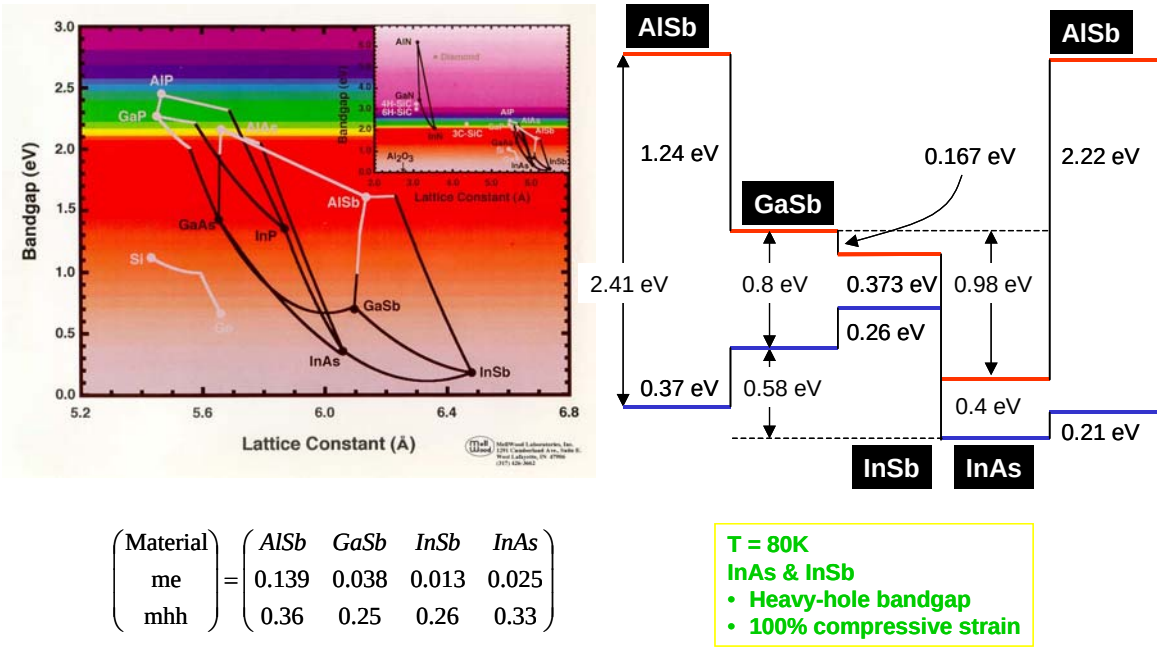

Material	AlSb	GaSb	InSb	InAs
me	0.139	0.038	0.013	0.025
mhh	0.36	0.25	0.26	0.33

T = 80K
InAs & InSb
- **Heavy-hole bandgap**
- **100% compressive strain**

Fig. 1: Type-II strained layer superlattice (SLS) material system: InAs/GaSb/AlSb and their energy bandgaps, lattice constants, energy band lineups, and carrier masses.

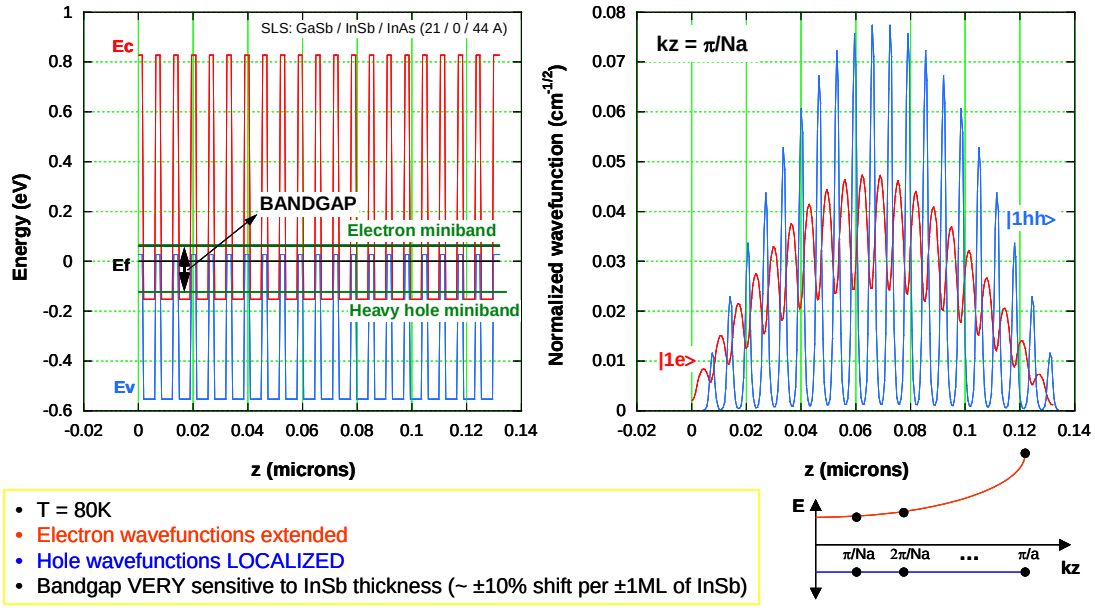

- T = 80K
- Electron wavefunctions extended
- Hole wavefunctions LOCALIZED
- Bandgap VERY sensitive to InSb thickness (~ ±10% shift per ±1ML of InSb)

Fig. 2: Quantum mechanical calculations showing SLS bandgap (left) and ground-state electron and hole wavefunctions (right) for a GaSb/InAs superlattice. Right figure shows confinement of electrons and holes in alternate layers, but with enough overlap to yield good light absorption. The wavefunction envelopes follow the dispersion relationship sketched on lower right.

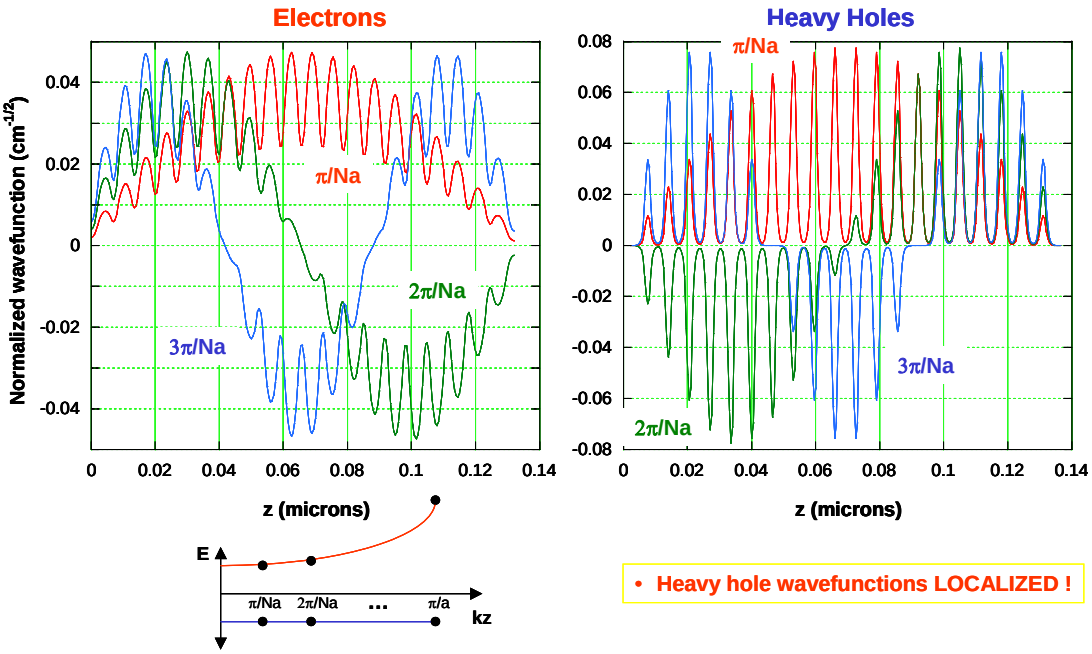

Fig. 3: First three wavefunctions for electrons (left) and heavy holes (right) showing localization of holes. This suggests that electrons should be the minority carriers so that their larger diffusion length translates to higher quantum efficiency. Wavefunction envelopes are modulated by the dispersion relationship sketched at the bottom.

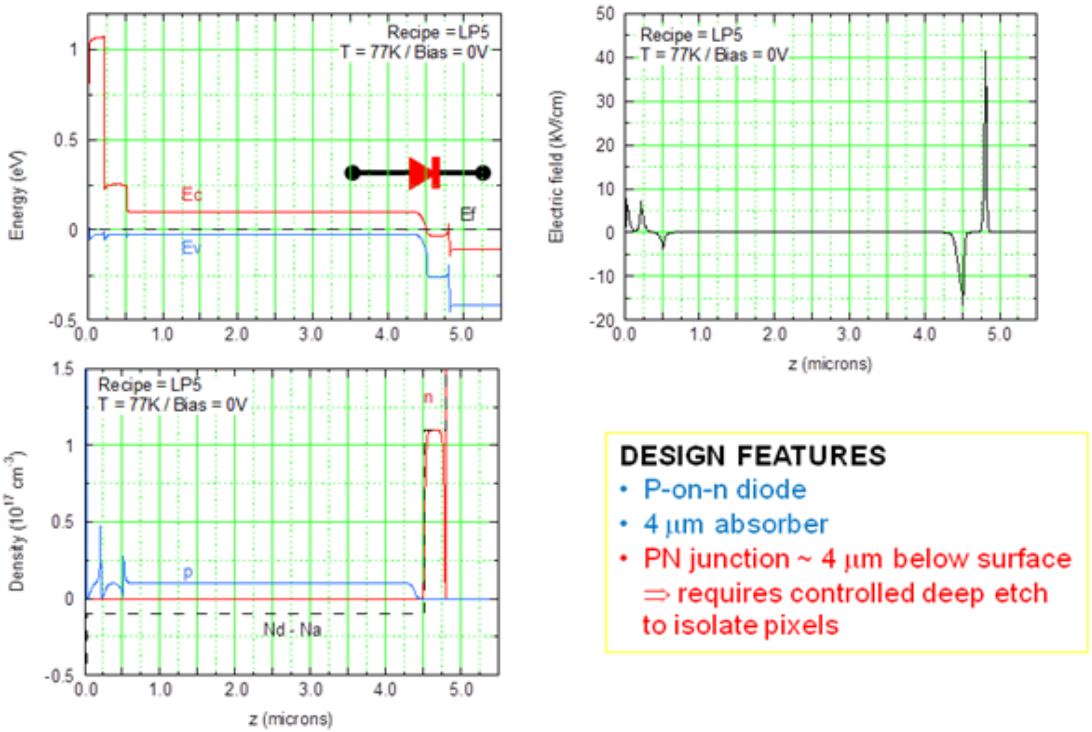

Fig. 4: Self-consistent energy band diagram (top left), electron (n) and hole (p) distributions (bottom left), and electric field (top right) for SLS diode at 77K.

3. SLS PHOTODIODE BAND DIAGRAM

The superlattice is selectively doped p and n type to produce a pn photodiode. Using Fermi-Dirac statistics and Poisson's equation iteratively, we calculate the self-consistent energy band diagram and carrier and electric field distributions at 77K for a pn diode with a p-doped absorber designed to have a longwave infrared bandgap (Fig. 4).

The depletion region at the pn junction determines diode capacitance, which is calculated to be ~ 0.4 pF for a 28 μm x 28 μm pixel. One point that emerges is that most of the absorber is flat-band, i.e. has zero electric field across it. This implies that photocurrent is generated mostly, not by drift, but by diffusion of minority carriers across the absorber.

4. SLS MATERIAL GROWTH AND CHARACTERIZATION

P-on-n SLS epitaxial (epi) material with the recipe modeled in Fig. 4 was grown by molecular beam epitaxy (MBE) on 2-inch GaSb substrates doped lightly n-type with Te. An average defect density of ~ 300/cm^2 was measured with a surface scan. While a bit higher than desirable, more work remains to be done to quantify what fraction of these actually knocks out pixels and renders them inoperable or bad.

MBE growth conditions and the InAs/GaSb interface chemistry were adjusted to achieve good lattice matching of epi to GaSb substrate, as evidenced by the strong satellite peaks and the small separation between the main SLS peaks and the GaSb substrate peak in the measured xray rocking curve (Fig. 5).

Spectral measurements on test devices fabricated from this material show a ~ 9.5 μm bandgap at 77K, in good agreement with our quantum-mechanical modeling.

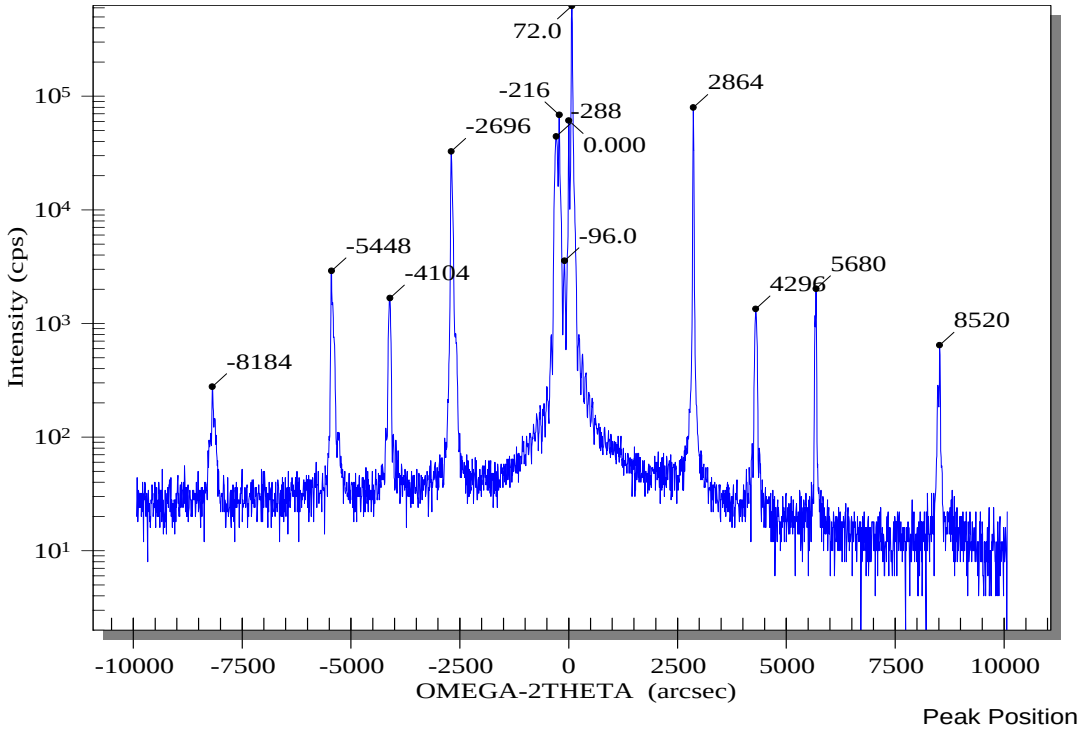

Fig. 5: Measured (004) xray rocking curve shows good SLS material quality – small separation between GaSb substrate peak and main superlattice peaks, and strong sharp satellite peaks.

5. SLS FPA FABRICATION

Detector arrays (1024x1024 format on 18 μm pitch) were printed on the SLS wafers with ~ 16 μm x 16 μm pixels defined by dry etching past the pn junction ~ 4 μm below the surface, ohmic contact metallization, passivation, and bumping with indium bumps.

After dicing, select die were hybridized (precision flip-chip bump-bonded) to matching bumped ISC0404 readout multiplexer die (FLIR Systems CVS). Each hybrid was underfilled and processed to have the GaSb substrate of the detector completely removed, leaving behind a ~ 5 μm thick detector membrane attached to the readout mux.

The resulting focal plane array (FPA) was mounted and wire-bonded in a leadless chip carrier (LCC) and tested for spectral, radiometric, signal-to-noise, and imaging performance.

6. SLS FPA PERFORMANCE

The measured spectral response of the FPA at 77K shows a cutoff ~ 9.5 μm and multiple peaks arising from optical resonances in the pixel cavity (Fig. 6). Knowing the cavity thickness, one can calculate the position of the various peaks, which turn out to agree closely with observations, as well as the "effective" refractive index of the superlattice, which exhibits little dispersion (see inset of Fig. 6). The step function shown in the figure is a spectrally-averaged value of the quantum efficiency (QE) that produces exactly the same photocurrent as the actual spectral response. Although it ignores the details of the shape of the spectral response, it provides a convenient metric to quantify the FPA's performance, the cutoff wavelength being the only required input parameter.

The spectrally-averaged QE is a function of reverse voltage bias across the photodiode. The mean value of the QE histogram for the 1024x1024 SLS FPA is plotted as a function of reverse bias in Fig. 7. It reaches ~ 50% at slight reverse bias and drops gently at higher bias (the reason for the drop is unknown at this time).

Note that the biases reported on the horizontal axis of Fig. 7 (as well as Fig. 8 and Fig. 9) are calculated from the actual bias words used during testing, as prescribed in the ISC0404 User's Guide. Any uncertainty affecting the correspondence between the two would result in a systematic offset (of unknown magnitude) of the true bias.

At the same time, the FPA-wide mean temporal noise equivalent difference in temperature (NEDT) reaches 30 mK at 77K and F/4 (Fig. 8).

The mean FPA dark current density ~ $2x10^{-4}A/cm^2$ attests to reasonably good bulk material quality and surface passivation (Fig. 9).

Pixel operability reaches 96% (good pixels defined as those with response within ±50% of mean value and NEDT < 2x mean value); most of the bad pixels are in an edge cluster which is expected to disappear with hybridization improvements.

The quality of the array is evident in the excellent imagery it produces (Fig. 10).

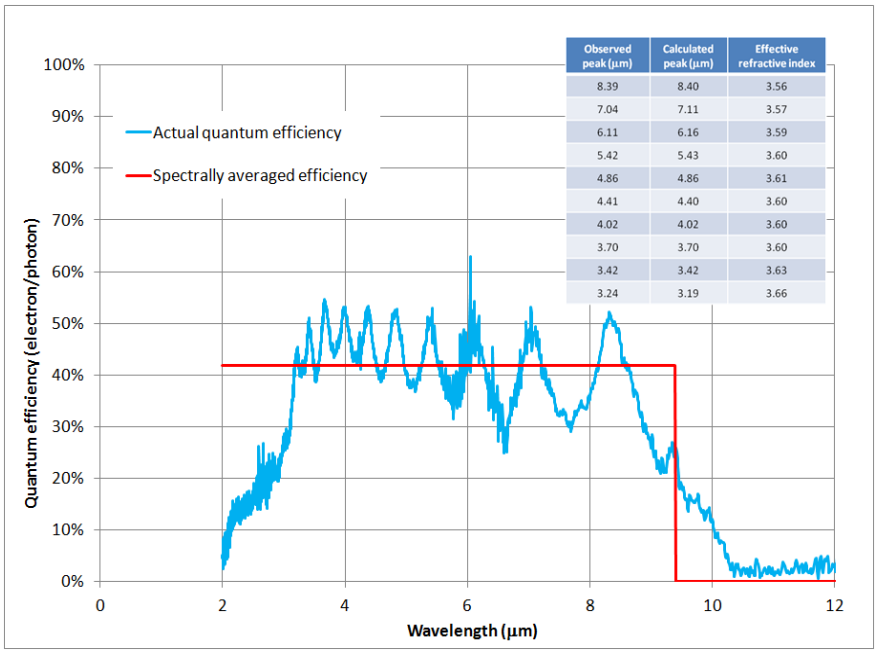

Observed peak (µm)	Calculated peak (µm)	Effective refractive index
8.39	8.40	3.56
7.04	7.11	3.57
6.11	6.16	3.59
5.42	5.43	3.60
4.86	4.86	3.61
4.41	4.40	3.60
4.02	4.02	3.60
3.70	3.70	3.60
3.42	3.42	3.63
3.24	3.19	3.66

Fig. 6: Measured spectral response of longwave infrared SLS FPA. The step function is a spectrally-averaged quantum efficiency (QE) value that produces the same photocurrent as the actual response. The peaks in the spectral response are due to optical resonances in the pixel cavity.

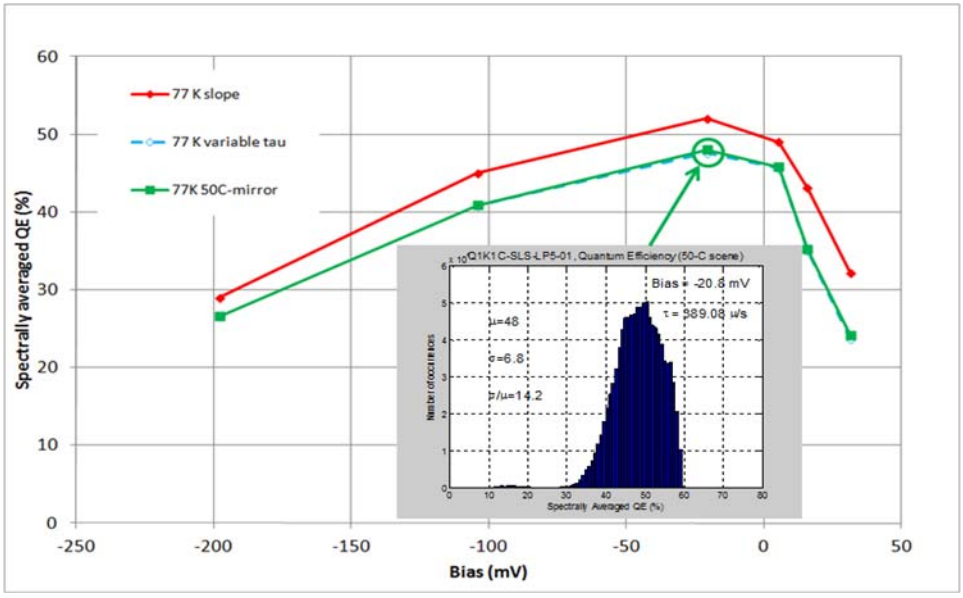

Fig. 7: Mean value of spectrally-averaged QE histogram of 1024x1024 SLS FPA measured by three different techniques hits ~ 50% at low reverse bias and 77K. AR coating will increase this value.

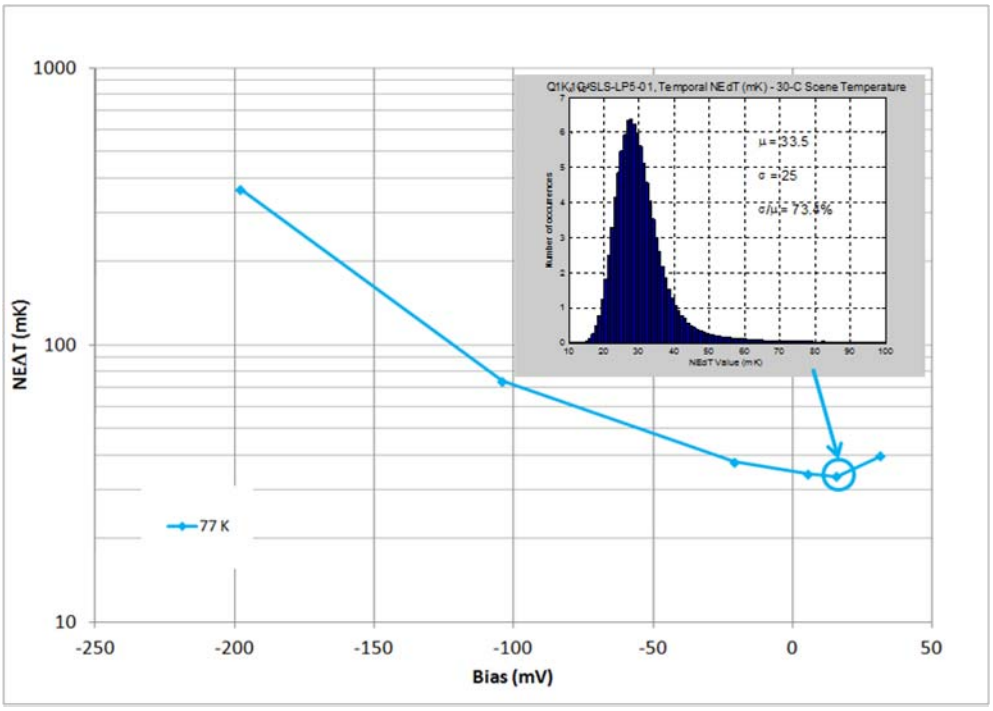

Fig. 8: Mean temporal NEDT of FPA reaches ~ 30 mK at 77K and using F/4 optics.

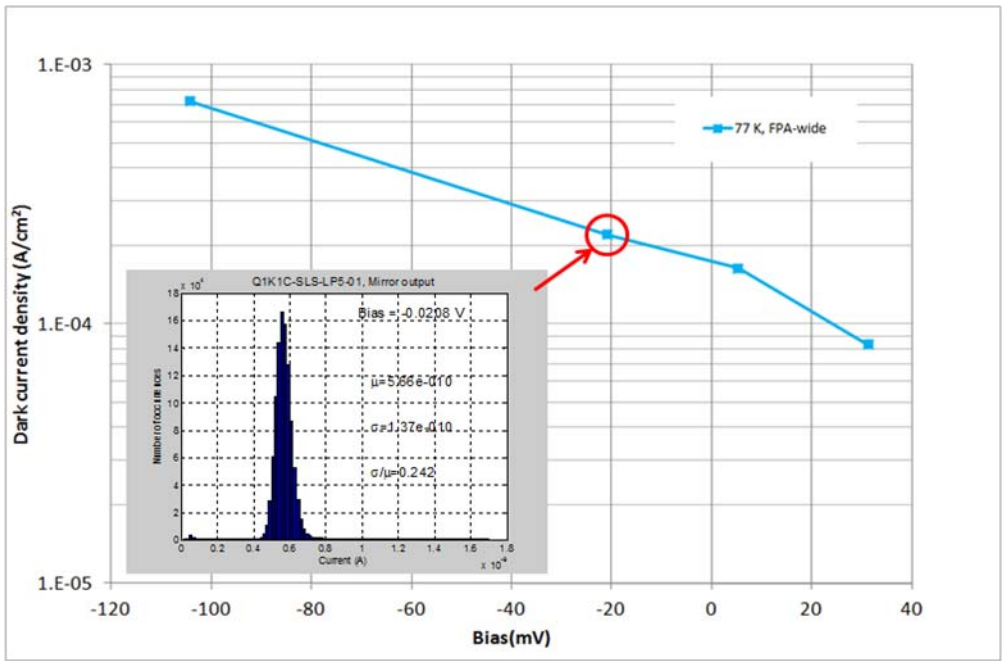

Fig. 9: FPA-wide mean dark current density ~ $2x10^{-4}$ A/cm^2 at the operating bias near 0V and 77K.

Fig. 10: Longwave infrared images from the 1024x1024 SLS FPA at 77K.

7. CONCLUSIONS

We have shown the viability and promise of Type-II InAs/GaSb SLS technology for making longwave infrared FPAs. FPAs with formats upto 1024x1024 on 18 μm pitch and cutoff ~ 9.5 μm have been demonstrated with good performance: quantum efficiency ~ 50%, NEDT ~ 30 mK (77K, F/4), and pixel operability ~ 96%. Longer cutoffs (11 μm) have been demonstrated in 320x256 FPAs. These achieve similar performance as above, but at a lower temperature of 68K.

Our future efforts in SLS will focus on extending the cutoff wavelength to 12 μm and developing a high-yield manufacturing process to enable SLS commercialization.

This new superlattice-based sensor technology shows how the III-V compound semiconductor industry can be harnessed to produce a high-performance cost-effective infrared imaging solution for the 21st century.

ACKNOWLEDGMENTS

We thank Meimei Tidrow, Sumith Bandara, Leslie Aitcheson, and Fenner Milton of NVESD, Lucy Zheng of IDA, Paul Pinsukanjana and Kevin Clark of IntelliEpi, Amy Liu and Dmitri Loubychev of IQE, Stefan Svensson of ARL, Sanjay Krishna of the University of New Mexico, Dan Manitakos of General Dynamics, Bob Keever of Boeing, Bob Benson of FLIR Systems, Murzy Jhabvala of NASA/GSFC, and Noah Clay of Harvard University for valuable technical discussions and feedback.

REFERENCES

[1] Sai-Halasz, G. A., Tu, R. and Esaki, L., "A new semiconductor superlattice," Appl. Phys. Lett. 30, 651-653 (1977).

[2] Sai-Halasz, G. A., Chang, L. L., Welter, J. –M., Chang, C. -A. and Esaki, L., "Optical absorption of $In_{1-x}Ga_xAs$-$GaSb_{1-y}As_y$ superlattices," Sol. St. Commun. 27, 935-937 (1978).

[3] Reine, M., “HgCdTe photodiodes for IR detection: a review,” Proc. SPIE 4288, 266 (2001).
[4] Ting, D. Z.-Y., Hill, C. J., Soibel, A., Keo, S. A., Mumolo, J. M., Nguyen, J. and Gunapala, S. D., "A high-performance long wavelength superlattice complementary barrier infrared detector," Appl. Phys. Lett. 95, 023508-023510 (2009).
[5] Delaunay, P. -Y., Nguyen, B. M., Hoffman, D., Huang, E. K. –W. and Razeghi, M., "Backgound limited performance of long wavelength infrared focal plane arrays fabricated from M-structure InAs-GaSb superlattices," IEEE J. Quantum Electron. 45, 157-162 (2009).
[6] Hill, C. J., Soibel, A., Keo, S. A., Mumolo, J. M., Gunapala, S. D., Rhiger, D. R., Kvaas, R. E. and Harris, S. F., "Infrared imaging arrays based on superlattice photodiodes," Proc. SPIE 6940, 69400C (2008).
[7] Kim, H. S., Plis, E., Rodriguez, J. B., Bishop, G. D., Sharma, Y. D., Dawson, L. R., Krishna, S., Bundas, J., Cook, R., Burrows, D., Dennis, R., Patnaude, K., Reisinger, A. and Sundaram, M., "Mid-IR focal plane array based on type-II InAs/GaSb strain layer superlattice detector with *nBn* design," Appl. Phys. Lett. 92, 183502-183504 (2008).
[8] Walther, M., Rehm, R., Fleissner, J., Schmiltz, J., Ziegler, J., Cabanski, W. and Breiter, R., "InAs/GaSb type-II short-period superlattices for advanced single and dual-color focal plane arrays," Proc. SPIE 6542, 654206 (2007).
[9] Vurgaftman, I., Aifer, E. H., Canedy, C. L., Tischler, J. G., Meyer, J. R., Warner, J. H., Jackson, E. M., Hildebrandt, G. and Sullivan, J. G., "Graded band gap for dark-current suppression in long-wave infrared W-structured type-II superlattice photodiodes," Appl. Phys. Lett. 89, 121114-121116 (2006).